

Article

Salt-Templated Platinum-Copper Porous Macrobeams for Ethanol Oxidation

F. John Burpo^{1,2,*} , Enoch A. Nagelli^{1,2} , Anchor R. Losch¹, Jack K. Bui¹, Gregory T. Forcherio³, David R. Baker³, Joshua P. McClure³, Stephen F. Bartolucci⁴ and Deryn D. Chu³

¹ Department of Chemistry and Life Science, United States Military Academy, West Point, NY 10996, USA

² Photonics Research Center, United States Military Academy, West Point, NY 10996, USA

³ United States Army Research Laboratory-Sensors and Electron Devices Directorate, Adelphi, MD 20783, USA

⁴ U.S. Army Combat Capabilities Development Command-Armaments Center, Watervliet, NY 12189, USA

* Correspondence: john.burpo@westpoint.edu; Tel.: +1-845-938-3900

Received: 1 July 2019; Accepted: 30 July 2019; Published: 2 August 2019



Abstract: Platinum nanomaterials provide an excellent catalytic activity for diverse applications and given its high cost, platinum alloys and bi-metallic nanomaterials with transition metals are appealing for low cost and catalytic specificity. Here the synthesis of hierarchically porous Pt–Cu macrobeams and macrotubes templated from Magnus’s salt derivative needles is demonstrated. The metal composition was controlled through the combination of $[\text{PtCl}_4]^{2-}$ with $[\text{Pt}(\text{NH}_3)_4]^{2+}$ and $[\text{Cu}(\text{NH}_3)_4]^{2+}$ ions in different ratios to form salt needle templates. Polycrystalline Pt–Cu porous macrotubes and macrobeams 10’ s–100’ s μm long with square cross-sections were formed through chemical reduction with dimethylamine borane (DMAB) and NaBH_4 , respectively. Specific capacitance as high as 20.7 F/g was demonstrated with cyclic voltammetry. For macrotubes and macrobeams synthesized from $\text{Pt}^{2-}:\text{Pt}^{2+}:\text{Cu}^{2+}$ salt ratios of 1:1:0, 2:1:1, 3:1:2, and 1:0:1, DMAB reduced 3:1:2 macrotubes demonstrated the highest ethanol oxidation peak currents of 12.0 A/g at 0.5 mV/s and is attributed to the combination of a highly porous structure and platinum enriched surface. Salt templates with electrochemical reduction are suggested as a rapid, scalable, and tunable platform to achieve a wide range of 3-dimensional porous metal, alloy, and multi-metallic nanomaterials for catalysis, sensor, and energy storage applications.

Keywords: platinum; copper; nanomaterials; porous; catalysis; fuel cells

1. Introduction

Platinum nanomaterials provide excellent catalytic activity for fuel cells, sensors, and automotive and petroleum applications [1,2]. Given the relative scarcity and high cost of platinum, platinum alloy nanostructures are appealing for materials scale-up and sustainability. Controlling platinum alloy composition and nanostructure shape allows the tuning of catalytic specificity [3–6]. High aspect ratio nanomaterials maximize catalytically active surface area while minimizing material volume, while alloy composition allows for control over chemical adsorbate binding and product release [7,8]. Furthermore, the relative solvent exposure of different platinum crystal faces also provides a means to control reaction kinetics [9]. While numerous platinum-palladium alloy nanostructures have been developed [10–13], platinum alloys and bi-metallic materials with abundant transition metals is appealing for low cost and tuning catalytic specificity [14–16].

Copper is an abundant, low-cost transition metal that has been used to synthesize platinum alloy and bimetallic nanomaterials. Pt–Cu nanomaterials synthesis techniques include dealloying [17], glucose-directed synthesis of alloy nanowire networks [18], electrodeposition [19],

cyclic electrodeposition of PtCu alloy porous electrodes [20], electrochemically synthesized Cu/Pt core-shell catalysts [21], and seed mediated interdiffusion [22]. Resulting Pt–Cu nanostructures include nanocubes [23], nanoboxes [24] nanodendrites [25,26], microwires [27], nanowires [28], core-shell nanowires [29], alloy nanocrystals [30,31], concave nanoframes [32], aligned nanoporous Pt–Cu bimetallic microwires [3], platinum–copper alloy nanocrystals supported on reduced graphene oxide [30], and 3-dimensional structures [33]. Primary applications for Pt–Cu nanomaterials include electro-oxidation of methanol and ethanol [34], oxygen reduction reaction [17,35,36], and glucose detection [37]. While numerous Pt–Cu nanostructures have been demonstrated, discrete nanoparticles require post-synthesis binding into functional electrodes, and there has been limited demonstration of scalable aqueous-based synthesis of porous 3-dimensional structures.

Recently rapid noble metal aerogel synthesis was demonstrated via a high concentration direct reduction approach [38,39], and salt templating was used to synthesize 2-dimensional materials [40,41]. Combining the use of high salt concentrations and salt templates, our group synthesized Pt and Pt–Pd macrobeams and porous nanomaterials from Magnus’s and Vauquelin’s salts and derivatives [42, 43], as well as salt-templated Au–Pd and Au–Cu–Pd multi-metallic porous materials [44]. Rapid precipitation of high-aspect ratio Magnus’s salts [45] and Vauquelin’s salts [46] results from the combination of oppositely charged square planar platinum and palladium metal ions, respectively. Vauquelin discovered pink salt needle formation with oppositely charged square planar palladium salts in 1813 [46]. Magnus later discovered analogous platinum green salt needle formation from the combination of oppositely charged square planar platinum ion complexes [45]. The previous studies demonstrating the use of Magnus’s salt derivative needles as nanostructure synthesis templates for 3-dimensional noble metal porous materials presents an opportunity for Pt–Cu bi-metallic and alloy materials synthesis that is aqueous based, rapid, scalable, and does not require additional materials for integration and device performance.

Here we demonstrate the synthesis of hierarchically porous Pt–Cu macrobeams and macrotubes through electrochemical reduction of Magnus’s salt derivatives, and their use for catalytic ethanol oxidation. Combining various ratios of $[\text{PtCl}_4]^{2-}$, $[\text{Pt}(\text{NH}_3)_4]^{2+}$, and $[\text{Cu}(\text{NH}_3)_4]^{2+}$ ions forms high aspect ratio bimetallic salt templates with lengths from 10’ s to 100’ s of micrometers. Porosity, nanoparticle structure, and metal composition is controlled through salt template ion ratio and selection of reducing agent. Chemical reduction of the Pt–Cu salt templates with dimethylamine borane results in macrotube structures, while reduction with sodium borohydride (NaBH_4) results in macrobeams with a porous structure throughout the beam cross section. Pt–Cu macrotubes and macrobeams exhibit porous sidewalls with square cross-sections and generally conform to the length of the salt template. Material characterization was performed with polarized optical microscopy, scanning electron microscopy, X-ray diffractometry (XRD), and X-ray photoelectron spectroscopy (XPS). Electrochemical characterization was performed with electrochemical impedance spectroscopy and cyclic voltammetry in 0.5 M H_2SO_4 electrolyte to assess hydrogen adsorption-desorption and electrochemically accessible surface area, as well as 1 M KOH/1 M ethanol to examine ethanol oxidation catalysis. Electrochemically reduced bimetallic and multi-metallic salt templates are envisioned to provide a synthesis route for a broad range of 3-dimensional hierarchical, high surface area catalysts.

2. Results and Discussion

2.1. Platinum-Copper Macrobeam Synthesis Scheme

To prepare Magnus’s salt needle derivatives, 100 mM solutions of K_2PtCl_4 , $\text{Pt}(\text{NH}_3)_4\text{Cl}_2 \cdot \text{H}_2\text{O}$, and $\text{Cu}(\text{NH}_3)_4\text{SO}_4 \cdot \text{H}_2\text{O}$ were prepared to provide $[\text{PtCl}_4]^{2-}$, $[\text{Pt}(\text{NH}_3)_4]^{2+}$, and $[\text{Cu}(\text{NH}_3)_4]^{2+}$ square planar ions, respectively. Salt solutions were mixed in varying $\text{Pt}^{2-}:\text{Pt}^{2+}:\text{Cu}^{2+}$ ratios such that the cation to anion ratio was 1:1. The $\text{Pt}^{2-}:\text{Pt}^{2+}:\text{Cu}^{2+}$ salt ratios used in this study were 1:0:1, 3:1:2, 2:1:1, and 1:1:0 corresponding to Pt:Cu stoichiometric ratios of 1:1, 2:1, 3:1, and 1:0, respectively. As shown in the scheme in Figure 1 and observed experimentally, the solution mixtures form high aspect ratio

salt needles rapidly within 1–2 s. The salt needles are then exposed to either 100 mM DMAB or NaBH_4 reducing agent to form macrotubes or macrobeams, respectively. Using the same synthesis scheme, $\text{Pd}(\text{NH}_3)_4\text{Cl}_2$ was used to precipitate salt needles with $\text{Pt}^{2-}:\text{Pd}^{2+}:\text{Cu}^{2+}$ ratios of 2:1:1 and 3:1:2, and subsequently reduced with 100 mM DMAB with 1:50 (*v/v*) salt needle solution to reducing agent (Figure S1).

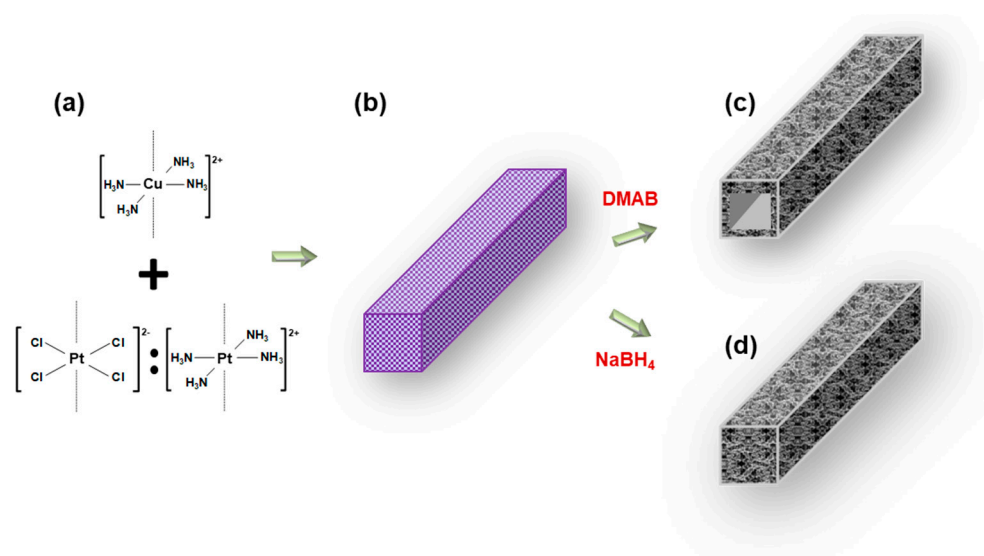


Figure 1. Platinum-copper porous macrotube–macrobeam synthesis scheme. (a) Addition of varying ratios of $[\text{Cu}(\text{NH}_3)_4]^{2+}$ with $[\text{PtCl}_4]^{2-}$ and $[\text{Pt}(\text{NH}_3)_4]^{2+}$. (b) Linear stacking of platinum and copper square planar complex ions to form Magnus’s salt crystal derivatives. (c,d) Reduction of platinum-copper salt needle templates to (c) square cross-section macrotubes using dimethylamine borane (DMAB), or (d) porous macrobeams using NaBH_4 .

As seen in Figure 2a, the salt needles present a purple color. Polarized optical microscopy was used to determine the salt needle lengths corresponding to each salt ratio shown in Figure 2b–d. Salts formed with a 1:0:1 ratio resulted in the longest salt needles ranging approximately 500 μm to more than 1000 μm . Salts formed with a 3:1:2 ratio are on the order of 100’s of μm with longer needles exceeding 500 μm . The 2:1:1 salt needles, are smaller ranging from 10’s of μm up to approximately 100 μm . 1:1:0 all platinum salt needles prepared from $[\text{PtCl}_4]^{2-}$ and $[\text{Pt}(\text{NH}_3)_4]^{2+}$, 100 mM solutions were previously reported as 20–65 μm [42]. The salt needle formation trend is a decrease in length as the relative copper ion content decreases. As the salt formation results from electrostatic attraction and square planar ion stacking, the larger salt needle precipitates with higher copper ion content is potentially attributed to an ion size mismatch between $[\text{Cu}(\text{NH}_3)_4]^{2+}$ with $[\text{PtCl}_4]^{2-}$.

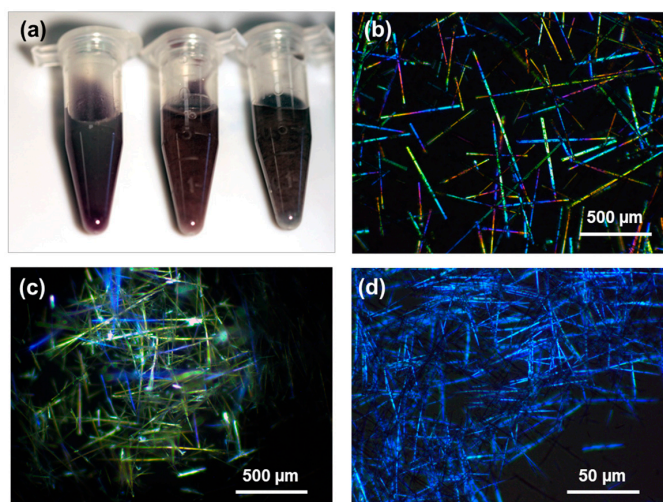


Figure 2. (a) Photograph of salt derivative templates. From left to right $\text{Pt}^{2-}:\text{Pt}^{2+}:\text{Cu}^{2+}$ ratios are 1:0:1, 2:1:1, and 3:1:2 Magnus's salt derivatives prepared from 100 mM salt solutions. Polarized optical microscope images of salt needle templates formed from $\text{Pt}^{2-}:\text{Pt}^{2+}:\text{Cu}^{2+}$ ratios of (b) 1:0:1, (c) 3:1:2, and (d) 2:1:1, 100 mM Magnus's salt derivatives.

2.2. Macrobeam Structure

2.2.1. Scanning Electron Microscopy (SEM)

Salt needles with $\text{Pt}^{2-}:\text{Pt}^{2+}:\text{Cu}^{2+}$ ratios of 1:0:1, 3:1:2, 2:1:1, and 1:1:0 were used as templates to synthesize hierarchically porous macrobeam structures through electrochemical reduction with either DMAB or NaBH_4 . DMAB reduced synthesis products are shown in Figure 3. In general, the resulting structures conform to the salt templates (Figures S2–S4). A distinct square cross-section is seen in the scanning electron microscope images for 1:0:1 in Figure 3a–c, 3:1:2 in Figure 3d–f, and 2:1:1 in Figure 3g–i. Additionally, these structures present a hollow core yielding a macrotube structure. The 1:1:0 salt template, however, does not present a distinct square cross-section or hollow-core when reduced with DMAB, but rather interconnected particles approximately 50 nm in diameter formed from smaller aggregated nanoparticles as seen in Figure 3j–l.

The macrotubes formed from DMAB reduced 1:0:1 $\text{Pt}^{2-}:\text{Pt}^{2+}:\text{Cu}^{2+}$ salt needles seen in Figure 3a–c have the largest and most distinct square cross-section with approximately 3 μm square sides. This larger square geometry, and corresponding linear dimension correlated with the polarized optical microscopy images in Figure 2b. The sidewalls appear to be aggregated nanoparticles forming a highly textured surface, but with a porosity that does not appear to extend laterally through the sidewalls. The macrotubes formed from 3:1:2 and 2:1:1 salts in Figures 3d–f and 3g–i, respectively, indicate a cross-section approximately 200 nm square, hollow cores, and sidewalls formed from interconnected nanoparticles that are porous from the exterior of the macrotubes to the inner hollow core. Using the same synthesis scheme, $\text{Pd}(\text{NH}_3)_4\text{Cl}_2$ was used to precipitate salt needles with $\text{Pt}^{2-}:\text{Pt}^{2+}:\text{Cu}^{2+}$ ratios of 2:1:1 and 3:1:2, subsequently reduced with 100 mM DMAB with 1:50 (*v/v*) salt needle solution to reducing agent (Figure S4), and presented structures similar to those seen in Figures 3d–f and 3g–i.

When salt needles with $\text{Pt}^{2-}:\text{Pt}^{2+}:\text{Cu}^{2+}$ ratios of 1:0:1, 3:1:2, 2:1:1, and 1:1:0 were reduced with NaBH_4 , the resulting structures shown in Figure 4 are distinctly different than those reduced with DMAB shown in Figure 3. In general, the macrobeam structures exhibit porosity from the network of interconnected nanoparticles, however, a distinct hollow core for the 1:0:1, 3:1:2, and 2:1:1 salt templates is not apparent. Two other features appear on the NaBH_4 reduced macrobeams that are not present on the DMAB reduced structures. The first feature, circled in yellow, is the appearance of linear striations that are orthogonal to the beam axis. The second feature, circled in red, is the appearance

of spheres that are connected to but distinct from the macrobeam structure. Energy-dispersive X-ray mapping shown in Figure S5 indicates that the spheres are composed of predominantly platinum. Similar spheres were previously observed for $\text{Pd}^{2+}:\text{Pt}^{2-}$ salts at a 1:1 ratio reduced with NaBH_4 [43].

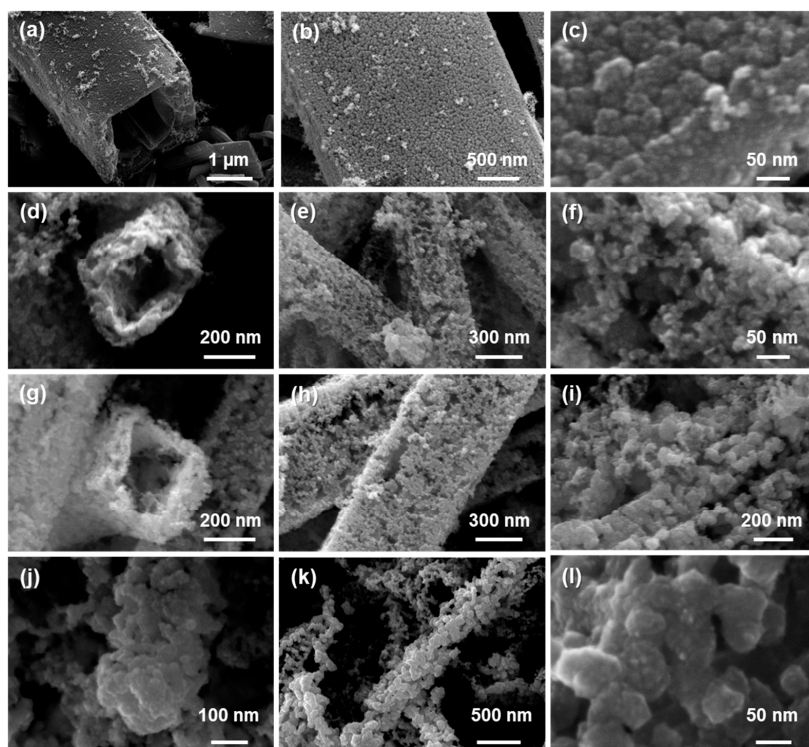


Figure 3. Scanning electron microscope images of platinum-copper macrotubes from 0.1 M DMAB reduced salts with $\text{Pt}^{2-}:\text{Pt}^{2+}:\text{Cu}^{2+}$ ratios of (a–c) 1:0:1, (d–f) 3:1:2, (g–i) 2:1:1, and (j–l) 1:1:0.

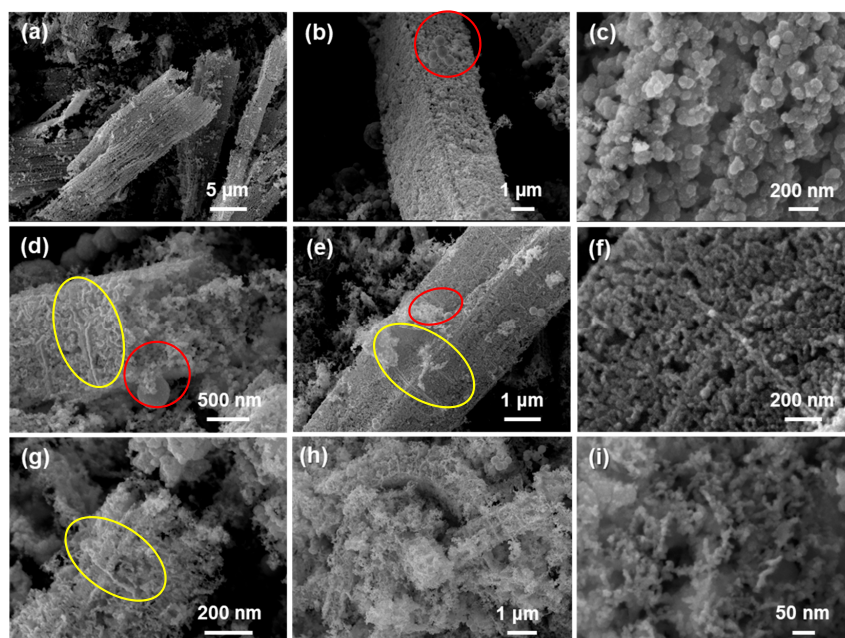
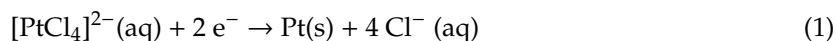


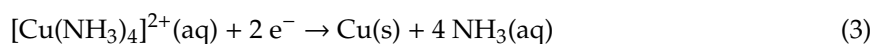
Figure 4. Scanning electron microscope images of platinum-copper macrobeam structures from 0.1 M NaBH_4 reduced salts with $\text{Pt}^-:\text{Pt}^{2+}:\text{Cu}^{2+}$ ratios of (a–c) 1:0:1, (d–f) 2:1:1, and (g–i) 3:1:2. Salts with a 1:1:0 ratio reduced with 0.1 M NaBH_4 were demonstrated in reference [42]. Linear striations are circled in yellow, and platinum nanospheres are circles in red.

2.2.2. Proposed Reduction-Dissolution Mechanism

The formation of a hierarchically porous macrobeam or macrotube from a salt needle template has been previously suggested to result from a charge balance dissolution mechanism during the reduction process [42]. In this study, the reduction of $[\text{PtCl}_4]^{2-}$ to Pt^0 shown in Equation (1) releases four Cl^- ions into solution near the salt template surface:



To maintain a charge balance for each $[\text{PtCl}_4]^{2-}$ ion reduced, it is thought that two $[\text{Pt}(\text{NH}_3)_4]^{2+}$ and/or $[\text{Cu}(\text{NH}_3)_4]^{2+}$ ions must dissolve into solution. The reduction of $[\text{Pt}(\text{NH}_3)_4]^{2+}$ to Pt^0 or $[\text{Cu}(\text{NH}_3)_4]^{2+}$ to Cu^0 shown in Equations (2) and (3) results in the release of four neutral ammonia molecules:



Ammonia's interaction with water is charge neutral in the formation of NH_4^+ and OH^- ions through its weakly basic nature. The proposed reduction-dissolution action and nanoparticle surface free energy minimization likely contributes to the porous structures observed in the SEM images in Figures 3 and 4.

2.2.3. X-ray Diffractometry

X-ray diffraction spectra for salt needles with $\text{Pt}^{2-}:\text{Pt}^{2+}:\text{Cu}^{2+}$ ratios of 1:0:1, 3:1:2, 2:1:1, and 1:1:0 reduced in 0.1 M DMAB and NaBH_4 are shown in Figure 5a,b, respectively. Diffraction peaks were indexed to Joint Committee on Powder Diffraction Standards (JCPDS) reference number 01-087-0640 for platinum (red dashed lines), and 03-065-9026 for copper (blue dashed lines). For both DMAB and NaBH_4 reduced 1:1:0 salt templates (all platinum), the peaks indexed well to 01-087-0640. As the copper content progressively increases from 2:1:1, 3:1:2, to 1:0:1, the DMAB reduced macrobeam diffraction peaks progressively shift to more intermediate positions between the indexed platinum and copper peaks suggesting possible alloy formation. The NaBH_4 platinum peaks, on the other hand, do not shift to intermediate positions between indexed Pt and Cu, but rather distinct 111 and 220 Cu peaks appear for the 1:0:1 samples with peak convolution broadening observed for the 2:1:1 and 3:1:2 samples peaks suggesting bimetallic structures.

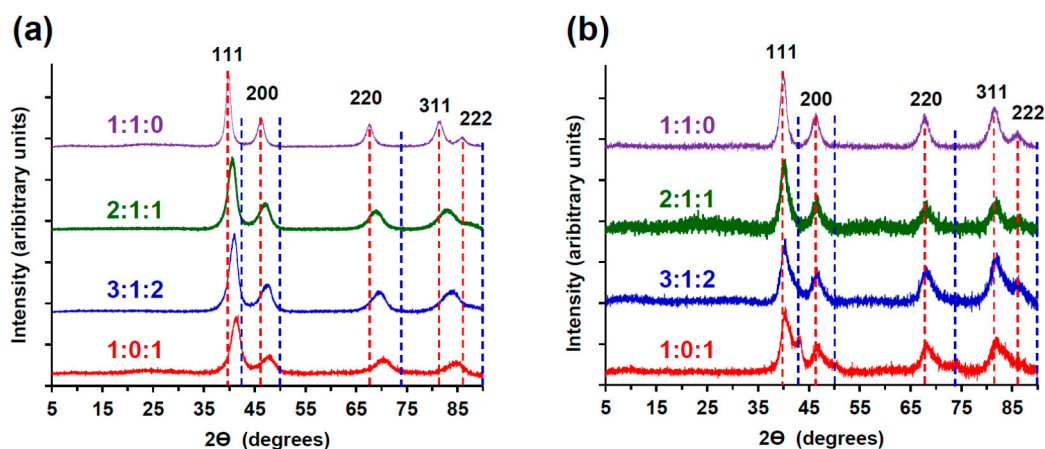


Figure 5. X-ray diffraction spectra of platinum-copper macrotubes-macrobeams reduced with (a) DMAB or (b) NaBH_4 from $\text{Pt}^{2-}:\text{Pt}^{2+}:\text{Cu}^{2+}$ salt ratios of 1:1:0, 2:1:1, 3:1:2, and 1:0:1. Peaks were indexed to JCPDS reference number 01-087-0640 for platinum (red dashed lines), and 03-065-9026 for copper (blue dashed lines).

2.2.4. X-ray Photoelectron Spectroscopy (XPS)

The elemental composition and phase of the Pt–Cu macrobeams formed with DAMB and NaBH₄ reducing agents were assessed by XPS. Figure 6 shows high-resolution XPS scans of the a,b Pt 4f and c,d Cu 2p regions at each Pt²⁺:Pt²⁺:Cu²⁺ ratio reduced by DAMB and NaBH₄. The Pt 4f_{7/2} and 4f_{5/2} photoelectron lines were measured at approximately 71 eV and 74 eV, respectively, with typical 3.33 eV spin-orbit separation, which indicated the metallic phase Pt (i.e., Pt⁰) [47]. The Cu 2p_{1/2} and 2p_{3/2} photoelectron features exhibited metallic, mono-, and di-valent Cu species (i.e., Cu⁰, Cu₂O, and CuO, respectively) [47] with relative concentrations dependent on the reduction agent. Satellite shake-up features observed at 942 eV, 944 eV, and 963 eV are predominantly associated with Cu⁺ (i.e., Cu₂O) [47]. The relative strength of DAMB versus NaBH₄ as a reductant for the Pt²⁺, Pt²⁺, and Cu²⁺ precursors resulted in varying distributions of presence in metallic and oxidized Pt/Cu phases with reductant-unique trends in measured binding energies.

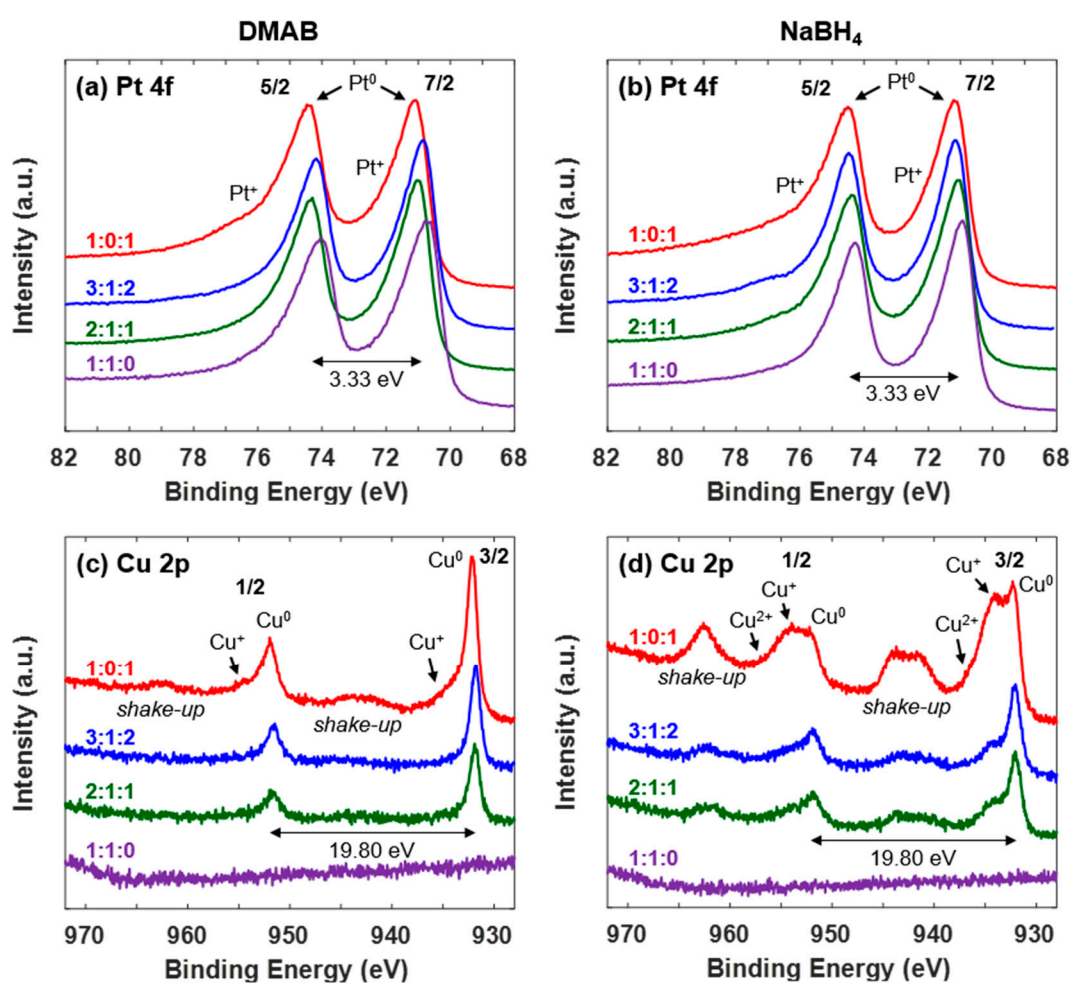


Figure 6. X-ray photoelectron spectra (XPS) for Pt–Cu macrobeams synthesized with Pt²⁺:Pd²⁺:Pt²⁺ salt template ratios of 1:0:1, 3:1:2, 2:1:1, and 1:1:0. (a,b) Normalized Pt 4f_{5/2} and Pt 4f_{7/2} and (c,d) Cu 2p_{1/2} and Cu 2p_{3/2} peaks for DMAB and NaBH₄ reduced salts, respectively.

Use of DAMB as a reductant resulted in samples with predominantly metallic Pt and Cu, with traces of Cu₂O confined to the 1:0:1 sample. The measured Pt 4f binding energies ranged from 70.7–71.1 eV for the 4f_{7/2} line and 74.0–74.4 eV for the 4f_{5/2} line, but did not appear to follow a linear trend with stoichiometric ratio. The DAMB-reduced 1:0:1 sample exhibited Pt⁺ signatures, which was consistent with the concomitant presence of Cu₂O (i.e., Cu⁺ 2p_{1/2} and 2p_{3/2} and shake-ups) in the Cu 2p spectrum.

The DMAB-reduced 3:1:2, 2:1:1, and 1:1:0 samples did not exhibit oxidized phases and appeared fully metallic.

Compared to DMAB, the use of NaBH₄ as a reductant resulted in samples with varying distributions of both metallic and oxidized Pt and Cu. Measured binding energies of the composite Pt 4f lines progressively decreased with Cu content, shifting the 4f_{7/2} line from 71.2 to 70.9 eV and the 4f_{5/2} line from 74.5 to 74.2 eV as the stoichiometric Cu percentage decreased from 50% to 0%. This was ostensibly attributable to the emergence of Pt⁺ species underlying the composite Pt 4f lines because oxidized Cu was evident in all samples (except for the 1:1:0 all platinum sample). The NaBH₄-reduced 2:1:1 and 3:1:2 samples exhibited Cu content that was predominantly in metallic Cu⁰ form and Cu⁺ state (i.e., Cu₂O). The NaBH₄-reduced 1:0:1 sample exhibited Cu that was less metallic in favor of the Cu⁺ oxidation state, while some appeared in the Cu²⁺ oxidation state (i.e., CuO).

Peak areas of the background-subtracted Pt 4f lines and Cu 2p_{3/2} lines were used to determine relative Pt and Cu atomic percentages (at %) and calculated Pt:Cu atomic ratios for comparison with EDS and precursor stoichiometry, shown in Table 1. The surface Cu content increased in the series 1:0:1 > 3:1:2 > 2:1:1 with Cu at % of 31% (52%), 15% (24%), and 11% (20%), respectively, for the DMAB (NaBH₄) reducing agent with ±1% uncertainty. The 1:1:0 samples contained no Cu. The balance was Pt and no contaminants were detected in the XPS survey scans, aside from C and O. Corresponding XPS Pt:Cu atomic ratios using DMAB (NaBH₄) were 1:0 (1:0), 7.9:1 (4.0:1), 5.8:1 (3.1:1), and 2.2:1 (0.92:1) for the Pt²⁻:Pt²⁺:Cu²⁺ samples 1:1:0 > 2:1:1 > 3:1:2 > 1:0:1, respectively. This followed the same general trend measured in bulk EDS measurements, though suggests greater platinum enrichment of the surface for both DMAB and NaBH₄ reduced samples. For both NaBH₄ and DMAB reduced samples, the EDS Pt:Cu ratios indicated less metalized Pt than was present stoichiometrically in the salt-template suggesting that the [Cu(NH₃)₄]²⁺ ion reduces preferentially in the given reducing conditions. This effect appears more pronounced for the NaBH₄ reduced samples. The closer correspondence of the DMAB reduced EDS Pt:Cu ratios to the salt-stoichiometry also correlates with the lesser presence of oxide species seen with XPS. Further, the reduction-dissolution mechanism suggested in Section 2.2.2 would make Pt ions available for reduction on the macrobeam particle surface once the charge gradients dissipate providing a possible reason surface enrichment of platinum observed with XPS.

Table 1. Atomic composition of Pt–Cu macrotubes and macrobeams reduced with NaBH₄ and DMAB, respectively.

	Pt ²⁻ :Pt ²⁺ :Cu ²⁺	Stoic. Pt:Cu	EDS Pt:Cu	XPS Pt:Cu
NaBH ₄	1:0:1	1:1	0.5:1	0.92:1
	3:1:2	2:1	1.3:1	3.1:1
	2:1:1	3:1	2.5:1	4.0:1
	1:1:0	1:0	1:0	1.0:0
DMAB	1:0:1	1:1	0.7:1	2.2:1
	3:1:2	2:1	1.5:1	5.8:1
	2:1:1	3:1	2.1:1	7.9:1
	1:1:0	1:0	1:0	1.0:0

2.3. Pt–Cu Macrobeam Electrochemical Characterization

2.3.1. Electrochemical Impedance Spectroscopy (EIS) in 0.5 M H₂SO₄

After chemical reduction of the Pt²⁻:Pt²⁺:Cu²⁺ salt needles with DMAB, the resulting Pt–Cu macrotubes were pressed between glass slides with approximately 200 kPa into free-standing films for electrochemical characterization. Electrochemical impedance spectroscopy was performed in 0.5 M H₂SO₄ in a frequency range of 1 MHz to 1 mHz, with the resulting Nyquist plots shown in Figure 7a. The macrobeam films from Pt²⁻:Pt²⁺:Cu²⁺ salt ratios of 1:1:0, 2:1:1, 3:1:2, and 1:0:1 exhibit characteristic high surface area capacitive behavior throughout the whole frequency range. Figure 7b shows the

high-frequency resistance through the macrotube films. The variation in the real axis intercept is due to minor differences in contact between the sample film and working electrode. In general, the samples present high-frequency impedance spectra consistent with porous samples [48,49]. A larger semi-circle from the charge transfer resistance for the 1:1:0 sample is possibly due to the less well connected macrobeam particles seen in Figure 3j–l. The DMAB samples charge transfer resistance is also attributed to the larger internal surface area within films for charge transport through the open network of macrotubes. Cyclic voltammetry (CV) of the $\text{Pt}^{2-}:\text{Pt}^{2+}:\text{Cu}^{2+}$ salt ratios of 1:1:0, 2:1:1, 3:1:2, and 1:0:1 was conducted in 0.5 M H_2SO_4 (Figure S8). Figure 7c shows the CV of Pt–Cu microbeams film from a 1:0:1 $\text{Pt}^{2-}:\text{Pt}^{2+}:\text{Cu}^{2+}$ salt ratio, in 0.5 M H_2SO_4 for scan rates of 1, 5, 10, 25, and 50 mV/s. The CV shows characteristic oxidation-reduction peaks and the hydrogen adsorption-desorption in the 1:0:1 macrotube film from the presence of catalytic platinum from the 2.2:1 atomic composition of Pt:Cu (as shown in the XPS results in Table 1). Moreover, Figure 7d shows the CV in 0.5 M H_2SO_4 at a 0.5 mV/s scan rate for the various DMAB reduced macrotube films with $\text{Pt}^{2-}:\text{Pt}^{2+}:\text{Cu}^{2+}$ salt ratios of 1:1:0, 2:1:1, 3:1:2, and 1:0:1. The CVs in Figure 7c,d indicate characteristic hydrogen adsorption and desorption peaks from the presence of platinum between -0.2 V and 0 V (vs Ag/AgCl). The electrochemical active surface areas determined from the capacitive region between 0.15–0.25 V for the 0.5 mV/s CV curves are 3.8, 10.5, 20.7, and 12.9 F/g for the macrotube films with $\text{Pt}^{2-}:\text{Pt}^{2+}:\text{Cu}^{2+}$ salt ratios of 1:1:0, 2:1:1, 3:1:2, and 1:0:1, respectively. In Figure 7d, the pronounced oxidation peak occurring around at +0.96 V (vs Ag/AgCl) and reduction peaks more positive than +0.58 V (vs Ag/AgCl) are associated with the overall catalytic bimetallic crystal structure in the different Pt:Cu films. The oxidation of Pt-H to Pt-OH and Pt-OH to Pt-O is evident in the strong oxidation peaks at +0.96 V (vs Ag/AgCl) and +1.1 V (vs Ag/AgCl), respectively [43]. The overall larger current density normalized for the mass of platinum ($\text{A}/\text{g}_{\text{Pt}}$) in the 2:1:1 salt ratio is a result of the contribution of catalytic current from the high atomic composition of platinum within the microtube film (as shown in the EDS and XPS results in Table 1). The hydrogen adsorption and desorption more negative than 0 V (vs Ag/AgCl) were more distinct in the macrotubes with the higher elemental composition of platinum (as shown in the EDS and XPS results in Table 1) and surface accessible catalytic sites within the network. The oxidation peaks observed at +0.58 V (vs Ag/AgCl) in both Figure 7c,d is attributed to a hydrogen spill over, the migration of chemisorbed hydrogen from the metal electrode onto glass support surfaces, as in the case of the electrochemical cell used in this study [50].

Using the hydrogen adsorption of the CV curves at 0.5 mV/s scan rates, a nominal value of $210 \mu\text{C}/\text{cm}^2$ for hydrogen adsorption on platinum [51], and the EDS determined sample mass composition, the electrochemically active surface areas (ECSA) for DMAB reduced 1:0:1, 3:1:2, 2:1:1, and 1:1:0 salts were 31.8, 22.6, 20.9, and $10.6 \text{ m}^2/\text{g}_{\text{Pt}}$, respectively. The corresponding ideal nanoparticle geometries based on the EDS mass averaged densities were 10.7, 13.8, 14.5, and 27.2 nm, respectively. These ideal nanoparticle geometries generally match the nanoparticle feature sizes observed in Figure 3 for each macrobeam Pt:Cu ratio.

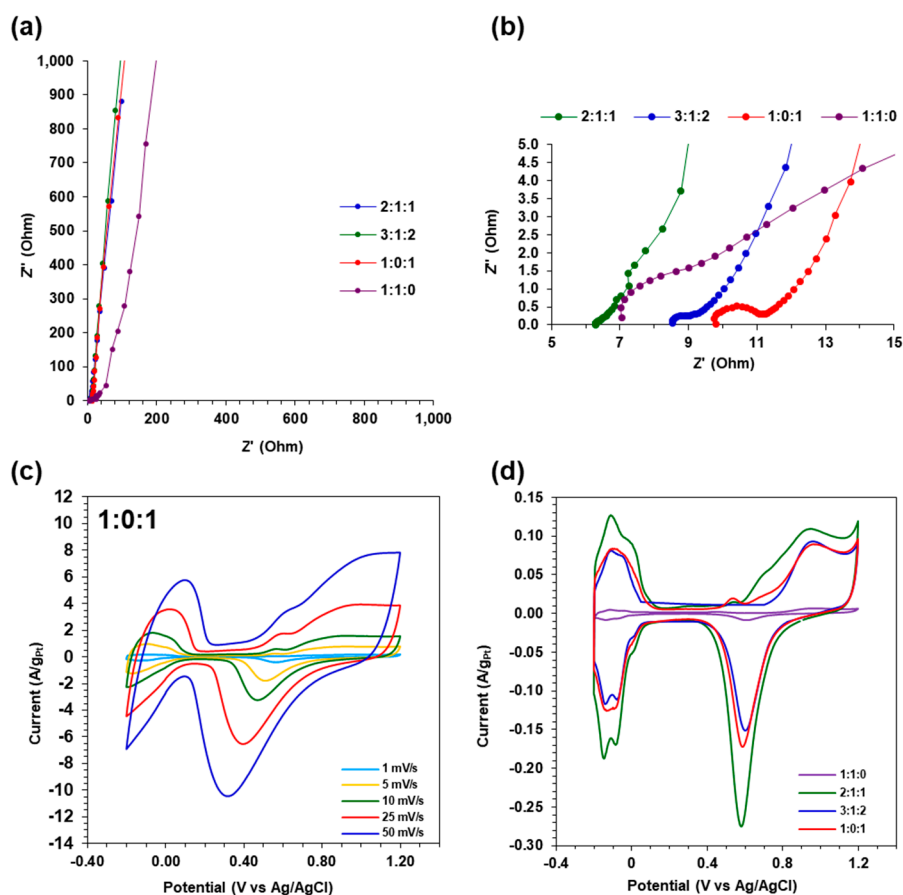
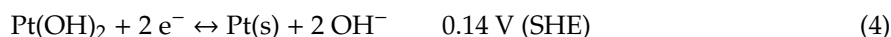


Figure 7. Electrochemical characterization of Pt–Cu macrotubes from $\text{Pt}^{2-}:\text{Pt}^{2+}:\text{Cu}^{2+}$ salts reduced with DMAB. (a) Electrochemical impedance spectroscopy (EIS) in 0.5 M H_2SO_4 at frequency range of 1 MHz to 1 mHz. (b) High-frequency EIS from (a); (inset) EIS spectrum for 1:1:0. (c) Cyclic voltammetry (CV) in 0.5 M H_2SO_4 for Pt–Cu macrobeams from a 1:0:1 $\text{Pt}^{2-}:\text{Pt}^{2+}:\text{Cu}^{2+}$ salt ratio, in 0.5 M H_2SO_4 for scan rates of 1, 5, 10, 25, and 50 mV/s. (d) CV in 0.5 M H_2SO_4 and 0.5 mV/s scan rate for macrotubes with $\text{Pt}^{2-}:\text{Pt}^{2+}:\text{Cu}^{2+}$ salt ratios of 1:1:0, 2:1:1, 3:1:2, and 1:0:1.

2.3.2. Ethanol Oxidation in 1 M KOH/1 M Ethanol

The catalytic performance for ethanol oxidation of the macrotube films from chemical reduction with DMAB (Figure 8a) and NaBH_4 (Figure 8b) from the various $\text{Pt}^{2-}:\text{Pt}^{2+}:\text{Cu}^{2+}$ salt ratios of 1:1:0, 2:1:1, 3:1:2, and 1:0:1 was evaluated with CV in 1 M KOH and 1 $\text{CH}_3\text{CH}_2\text{OH}$. The electrooxidation of ethanol can result in the formation of acetylaldehyde and ultimately acetic acid [52]. Both of the CVs in Figure 8 have discrete oxidation peaks in the forward scan from the oxidation of the adsorbed ethanol and a reverse cathodic scan with another corresponding oxidation peak due to the oxidation of partially oxidized intermediate species such as CO, CH_3COO^- , and CH_3CO^- [34,53]. As seen in both Figures 8a and 8b, the ethanol oxidation peaks in both the forward and reverse scans for the different $\text{Pt}^{2-}:\text{Pt}^{2+}:\text{Cu}^{2+}$ salt ratio macrobeam-macrotube films varied due to the differences in the amount of accessible catalytic platinum atomic sites as confirmed by EDS and XPS. Figure 8a shows the CV for the Pt–Cu macrotube films produced by chemical reduction with DMAB, the electrooxidation of ethanol for the $\text{Pt}^{2-}:\text{Pt}^{2+}:\text{Cu}^{2+}$ salt ratio macrotube films varied between -0.27 V to -0.13 V (Ag/AgCl) in the forward anodic scans. The same variation was observed in the NaBH_4 reduced $\text{Pt}^{2-}:\text{Pt}^{2+}:\text{Cu}^{2+}$ salt ratio macrobeam films where the ethanol oxidation peaks occurred in between -0.40 V (vs Ag/AgCl) to -0.26 V (Ag/AgCl) in the forward anodic scans. Meanwhile, on the reverse cathodic scan, the remaining surface oxides and intermediates are reduced until the potential is too negative to oxidize the remaining adsorbed species as represented by the sharp oxidation followed by reduction current peaks [52].

The sharp stripping peaks observed at approximately -0.2 V (vs Ag/AgCl) are attributed to the reduction of $\text{Pt}(\text{OH})_2$ shown in Equation (4),



and adsorbed OH and O species similar to those observed on palladium catalysts [54]. The reverse cathodic scans on both Figures 8a and 8b for 1:0:1 have multiple oxidation and reduction current peaks likely due to having the highest atomic composition of copper.

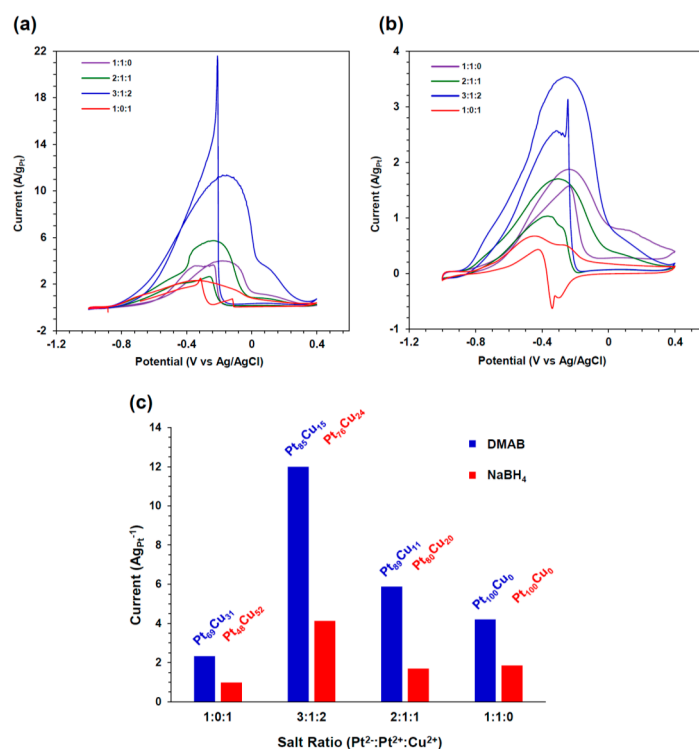


Figure 8. Ethanol oxidation peak currents (A/g_{Pt}) in 1 M KOH and 1 M ethanol at 0.5 mV/s for $\text{Pt}^{2+}:\text{Pt}^{2+}:\text{Cu}^{2+}$ salt ratios of 1:1:0, 2:1:1, 3:1:2, and 1:0:1 reduced in (a) DMAB and (b) NaBH_4 . (c) Volcano plot from data in (a) and (b) with Pt_xCu_y mass ratios; DMAB (blue) and NaBH_4 (red).

Figure 8c shows a volcano plot with data from Figure 8a,b. Macrobeams-macrotubes prepared from the 3:1:2 salts show the highest ethanol oxidation currents relative to the other samples. There is a general increase in peak oxidation current from the 1:1:0 to 2:1:1 and then the 3:1:2 samples, with a significant drop-off with the 1:0:1 samples. This trend is attributed to the balance of high surface area, phase composition, and surface platinum enrichment see in SEM, XRD, and XPS data. DMAB reduced samples yielded higher ethanol oxidation currents than the NaBH_4 reduced samples and is attributed to the greater presence of surface oxide species on the NaBH_4 reduced samples seen with XPS.

While the ECSA values of the Pt–Cu samples in H_2SO_4 electrolyte corresponds to the particle feature sizes observed with SEM, and is comparable to other Pt–Cu studies, ethanol oxidation performance comparison to previous Pt–Cu studies is challenging as the free-standing films and electrode conditions in this work are unique. Unlike dispersed materials in direct contact with a glassy carbon electrode conventionally used, the hierarchical porosity of the entangled macrobeams-macrotubes of the free-standing films, and sample mass of approximately 1–5 mg, introduced hysteresis attributable to current distribution, charging current, and mass transfer effects so that the performance at a slower scan rate of 0.5 mV/s is reported in Figure 8. The DMAB reduced 3:1:2 macrotubes exhibited the highest peak ethanol oxidation current of 12.0 A/g at 0.5 mV/s. As an indirect comparison, Pt/C and

PtCu_{1.8} screw thread-like platinum–copper nanowires had reported ethanol oxidation peak currents of 0.21 A/mg_{Pt} (210 A/g_{Pt}) and 0.25 A/mg_{Pt} (250 A/g_{Pt}) at 50 mV/s, respectively.

The assembly of practical electrodes for actual device integration and performance is a key step in realizing the benefits of nanoscale materials. Some of the attractive aspects of the salt-templated Pt–Cu macrotubes-macrobeams are the rapid precipitation of the salt needle templates, the one-step reduction synthesis, and the ability to press the Pt–Cu nanostructures into free-standing films for direct device integration. These considerations are envisioned to facilitate scale-up of salt-templated nanomaterials. One key challenge in the scale-up process using mechanical pressing to assemble entangled macrotubes is to ensure homogeneous active material and pore size distribution throughout the thickness and volume of the electrode.

3. Materials and Methods

3.1. Copper-Platinum Macrobeam Synthesis

Magnus' Pt–Cu salt needle derivatives were prepared by mixing 100 mM square planar cation complexes to anion complexes at 1:1 (*v/v*). The 100 mM platinum and copper salts used were Pt(NH₃)₄Cl₂•H₂O, K₂PtCl₄, and Cu(NH₃)₄SO₄•H₂O (Sigma Aldrich, USA). Salt needle templates were formed by combining solutions in Pt²⁺:Pt²⁺:Cu²⁺ stoichiometric ratios of 1:1:0, 2:1:1, 3:1:2, and 1:0:1. A total of 1 mL salt solution was prepared, and then reduced with either DMAB or NaBH₄ (Sigma Aldrich, USA) in a 1:50 (*v/v*) salt needle solution to reducing agent. Reduced platinum-copper macrotubes and macrobeams were rinsed in excess deionized water and dried at either ambient temperature or 100 °C. Using the same procedure Pd(NH₃)₄Cl₂ was used to precipitate salt needles with Pt²⁺:Pd²⁺:Cu²⁺ ratios of 2:1:1 and 3:1:2, subsequently reduced with 100 mM DMAB with 1:50 (*v/v*) salt needle solution to reducing agent (Figure S2).

3.2. Polarized Optical Microscopy

Polarized optical microscopy with an AmScope PZ300JC polarized light microscope (AmScope, Irvine, CA, USA) was used to image salt templates. Salt needle lengths were measured using ImageJ [55].

3.3. Scanning Electron Microscopy

Pt–Cu macrotubes and macrobeams were imaged with a FEI Helios 600 scanning electron microscope (SEM) (Thermo Fisher Scientific, Hillsboro, OR, USA). Energy dispersive X-ray spectroscopy (EDS) was performed with a FEI Helios 600 and a JEOL IT500HRLA SEM (JEOL USA, Peabody, MA USA).

3.4. X-ray Diffractometry

A PANalytical Empyrean diffractometer (PANalytical, Almelo, Netherlands) was used to collect X-ray diffractometry (XRD) spectra. Diffraction angles (2θ) from 5° to 90°, with a 2θ step size of 0.0130°, and 20 s per step were used at 45 kV and 40 mA with Cu K_α radiation (1.54060 Å). High Score Plus software (PANalytical) was used for XRD spectra analysis.

3.5. X-ray Photoelectron Spectroscopy

X-ray photoelectron spectroscopy (XPS) was performed on a ULVAC PHI VersaProbe III (Physical Electronics, East Chanhassen, MN USA) with a monochromated Al K_α source with a 100 μm spot, 25 W X-ray beam and 45° take-off angle. The operating pressure was < 6 × 10⁻⁶ Pa. Surface charging was neutralized by a low-voltage Ar-ion beam and a barium oxide electron neutralizer. Analyzer pass energy was set to 55 eV for high-resolution scans. All analysis was conducted with PHI's software MultiPak v.9.6.0.15. Spectra were corrected according to the adventitious C 1s peak at 284.8 eV binding energy. Relative Pt and Cu ratios were evaluated for each Pt–Cu macrobeam sample using Shirley background-corrected Pt 4f and Cu 2p_{3/2} peak areas.

3.6. Electrochemical Characterization

Macrobeams were pressed between glass slides with approximately 200 kPa into free-standing film electrochemical testing. A Bio-Logic VMP-3 potentiostat (Bio-Logic, Knoxville, TN, USA) was used to perform electrochemical impedance spectroscopy (EIS) and cyclic voltammetry (CV). An Ag/AgCl reference electrode, a 1 mm platinum wire counter-electrode, and a lacquer-coated 1 mm platinum wire with exposed tip in contact with samples were used in a three-electrode cell with 0.5 M H₂SO₄ electrolyte. EIS was performed at open-circuit voltage with a frequency range of 1 MHz to 1 mHz with a 10 mV sine wave. CV was performed in a voltage range of −0.2 to 1.2 V (vs. Ag/AgCl) with scan rates of 0.5, 1, 5, 10, 25, 50, 75, and 100 mV/s. Ethanol oxidation cyclic voltammetry was performed using 1 M KOH and 1 M ethanol with scan rates of 0.5, 1, 5, 10, 25, and 50 mV/s.

4. Conclusions

Here we demonstrated the synthesis of hierarchically porous Pt–Cu bimetallic macrobeams and macrotubes templated from Magnus's salt derivative needles. The metal composition was controlled through the combination of [PtCl₄]^{2−} with [Pt(NH₃)₄]²⁺ and [Cu(NH₃)₄]²⁺ ions in different ratios to form the salt needle templates. Polycrystalline Pt–Cu porous macrotubes and macrobeams with square cross-sections were formed through chemical reduction with DMAB and NaBH₄, respectively. Platinum enrichment on the nanoparticle surfaces was observed for DMAB reduced salts, whereas reduction with NaBH₄ resulted in small amounts of copper oxide species on the macrobeam surface. Electrochemical impedance spectroscopy indicated highly capacitive materials with electrochemical active surface area as high as 20.7 F/g demonstrated with cyclic voltammetry. For the characterized macrotubes and macrobeams synthesized from Pt^{2−}:Pt²⁺:Cu²⁺ salt ratios of 1:1:0, 2:1:1, 3:1:2, and 1:0:1, DMAB reduced 3:1:2 macrotubes demonstrated the highest ethanol oxidation peak currents of 12.0 A/g at 0.5 mV/s and is attributed to the combination of a highly porous structure for favorable mass transfer properties, and the platinum enriched surface. The use of salt templates with electrochemical reduction is suggested as an aqueous-based, rapid, scalable, and tunable platform to achieve a wide range of 3-dimensional porous metal, metal alloy, and multi-metallic nanomaterials for catalysis, sensor, and energy storage applications.

Supplementary Materials: The following are available online at <http://www.mdpi.com/2073-4344/9/8/662/s1>: Figure S1: Macrobeam synthesis scheme, Figure S2: SEM images of Pt–Cu macrobeams from Pt^{2−}:Pd²⁺:Cu²⁺ salts reduced with DMAB, Figure S3: SEM images of Pt–Cu macrobeams from Pt^{2−}:Pt²⁺:Cu²⁺ salts reduced with DMAB, Figure S4: SEM images of Pt–Cu macrobeams from Pt^{2−}:Pt²⁺:Cu²⁺ salts reduced with DMAB and NaBH₄, Figure S5: EDS mapping of macrobeams, Figure S6: (XPS) valence-band spectra, Figure S7: Electrochemical characterization of Pt–Cu macrobeams from Pt^{2−}:Pt²⁺:Cu²⁺ salts reduced with NaBH₄, Figure S8: CV in H₂SO₄ of Pt–Cu macrobeams from DMAB reduced salts, Figure S9: CV in 1 M KOH and 1 M ethanol of Pt–Cu macrobeams from DMAB reduced salts, Figure S10: CV in H₂SO₄ of Pt–Cu macrobeams from NaBH₄ reduced salts, Figure S11: CV in 1 M KOH and 1 M ethanol of Pt–Cu macrobeams from NaBH₄ reduced salts.

Author Contributions: Conceptualization, F.J.B. and J.P.M.; data curation, F.J.B., E.A.N., A.R.L., J.K.B., G.T.F., and D.R.B.; formal analysis, F.J.B. and E.A.N.; funding acquisition, F.J.B.; investigation, F.J.B., E.A.N., A.R.L., J.K.B., G.T.F., D.R.B., and S.F.B.; methodology, F.J.B., E.A.N., A.R.L., and J.K.B.; project administration, F.J.B.; resources, F.J.B. and S.F.B.; supervision, F.J.B. and D.D.C.; validation, E.A.N.; writing—original draft, F.J.B., E.A.N., G.T.F., and D.R.B.; writing—review and editing, F.J.B., E.A.N., J.P.M., S.F.B., and D.D.C.

Funding: This research and development effort was sponsored by Joint Center Picatinny located at Picatinny Arsenal, NJ, MIPR 11217514.

Acknowledgments: The authors would like to thank Joshua Maurer for the use of the FIB-SEM at Benet Laboratories, and Lance Richardson for his assistance with polarized optical microscopy at the United States Military Academy.

Conflicts of Interest: The authors declare no conflict of interest.

References

1. Chen, A.; Holt-Hindle, P. Platinum-Based Nanostructured Materials: Synthesis, Properties, and Applications. *Chem. Rev.* **2010**, *110*, 3767–3804. [[CrossRef](#)] [[PubMed](#)]
2. Peng, Z.; Yang, H. Designer platinum nanoparticles: Control of shape, composition in alloy, nanostructure and electrocatalytic property. *Nano Today* **2009**, *4*, 143–164. [[CrossRef](#)]
3. Qiu, X.; Dai, Y.; Zhu, X.; Zhang, H.; Wu, P.; Tang, Y.; Wei, S. Template-engaged synthesis of hollow porous platinum–palladium alloy nanospheres for efficient methanol electro-oxidation. *J. Power Sources* **2016**, *302*, 195–201. [[CrossRef](#)]
4. Yamauchi, Y.; Tonegawa, A.; Komatsu, M.; Wang, H.; Wang, L.; Nemoto, Y.; Suzuki, N.; Kuroda, K. Electrochemical Synthesis of Mesoporous Pt–Au Binary Alloys with Tunable Compositions for Enhancement of Electrochemical Performance. *J. Am. Chem. Soc.* **2012**, *134*, 5100–5109. [[CrossRef](#)] [[PubMed](#)]
5. Zhang, G.; Sun, S.; Cai, M.; Zhang, Y.; Li, R.; Sun, X. Porous dendritic platinum nanotubes with extremely high activity and stability for oxygen reduction reaction. *Sci. Rep.* **2013**, *3*, 1526. [[CrossRef](#)]
6. Chen, J.; Lim, B.; Lee, E.P.; Xia, Y. Shape-controlled synthesis of platinum nanocrystals for catalytic and electrocatalytic applications. *Nano Today* **2009**, *4*, 81–95. [[CrossRef](#)]
7. Liu, L.; Pippel, E.; Scholz, R.; Gösele, U. Nanoporous Pt–Co Alloy Nanowires: Fabrication, Characterization, and Electrocatalytic Properties. *Nano Lett.* **2009**, *9*, 4352–4358. [[CrossRef](#)]
8. Stamenkovic, V.R.; Mun, B.S.; Arenz, M.; Mayrhofer, K.J.J.; Lucas, C.A.; Wang, G.; Ross, P.N.; Markovic, N.M. Trends in electrocatalysis on extended and nanoscale Pt-bimetallic alloy surfaces. *Nat. Mater.* **2007**, *6*, 241–247. [[CrossRef](#)]
9. Stamenkovic, V.R.; Fowler, B.; Mun, B.S.; Wang, G.; Ross, P.N.; Lucas, C.A.; Marković, N.M. Improved Oxygen Reduction Activity on Pt₃Ni(111) via Increased Surface Site Availability. *Science* **2007**, *315*, 493–497. [[CrossRef](#)]
10. Wei, L.; Paramaconi, R.; Lars, B.; Annette, F.; Jipei, Y.; Anne-Kristin, H.; Dorin, G.; Zhikun, Z.; Stefan, K.; Nikolai, G.; et al. Bimetallic Aerogels: High-Performance Electrocatalysts for the Oxygen Reduction Reaction. *Angew. Chem. Int. Ed.* **2013**, *52*, 9849–9852.
11. Lim, B.; Wang, J.; Camargo, P.H.C.; Cogley, C.M.; Kim, M.J.; Xia, Y. Twin-Induced Growth of Palladium–Platinum Alloy Nanocrystals. *Angew. Chem. Int. Ed.* **2009**, *48*, 6304–6308. [[CrossRef](#)] [[PubMed](#)]
12. Lim, B.; Jiang, M.; Camargo, P.H.C.; Cho, E.C.; Tao, J.; Lu, X.; Zhu, Y.; Xia, Y. Pd–Pt Bimetallic Nanodendrites with High Activity for Oxygen Reduction. *Science* **2009**, *324*, 1302–1305. [[CrossRef](#)] [[PubMed](#)]
13. Zheng, J.-N.; He, L.-L.; Chen, F.-Y.; Wang, A.-J.; Xue, M.-W.; Feng, J.-J. Simple one-pot synthesis of platinum–palladium nanoflowers with enhanced catalytic activity and methanol-tolerance for oxygen reduction in acid media. *Electrochim. Acta* **2014**, *137*, 431–438. [[CrossRef](#)]
14. Anniyev, T.; Kaya, S.; Rajasekaran, S.; Ogasawara, H.; Nordlund, D.; Nilsson, A. Tuning the Metal–Adsorbate Chemical Bond through the Ligand Effect on Platinum Subsurface Alloys. *Angew. Chem. Int. Ed.* **2012**, *51*, 7724–7728. [[CrossRef](#)]
15. Cui, C.; Gan, L.; Li, H.-H.; Yu, S.-H.; Heggen, M.; Strasser, P. Octahedral PtNi Nanoparticle Catalysts: Exceptional Oxygen Reduction Activity by Tuning the Alloy Particle Surface Composition. *Nano Lett.* **2012**, *12*, 5885–5889. [[CrossRef](#)]
16. Zhou, W.-P.; Yang, X.; Vukmirovic, M.B.; Koel, B.E.; Jiao, J.; Peng, G.; Mavrikakis, M.; Adzic, R.R. Improving Electrocatalysts for O₂ Reduction by Fine-Tuning the Pt–Support Interaction: Pt Monolayer on the Surfaces of a Pd₃Fe(111) Single-Crystal Alloy. *J. Am. Chem. Soc.* **2009**, *131*, 12755–12762. [[CrossRef](#)] [[PubMed](#)]
17. Koh, S.; Strasser, P. Electrocatalysis on Bimetallic Surfaces: Modifying Catalytic Reactivity for Oxygen Reduction by Voltammetric Surface Dealloying. *J. Am. Chem. Soc.* **2007**, *129*, 12624–12625. [[CrossRef](#)] [[PubMed](#)]
18. Zhang, W.; Dong, Q.; Lu, H.; Hu, B.; Xie, Y.; Yu, G. Glucose-directed synthesis of Pt–Cu alloy nanowires networks and their electro-catalytic performance for ethylene glycol oxidation. *J. Alloys Compd.* **2017**, *727*, 475–483. [[CrossRef](#)]
19. Baumgärtner, M.E.; Raub, J. The Electrodeposition of Platinum and Platinum Alloys. *Platinum Met. Rev.* **1988**, *32*, 188–197.
20. Kloke, A.; Köhler, C.; Gerwig, R.; Zengerle, R.; Kerzenmacher, S. Cyclic Electrodeposition of PtCu Alloy: Facile Fabrication of Highly Porous Platinum Electrodes. *Adv. Mater.* **2012**, *24*, 2916–2921. [[CrossRef](#)]

21. Wei, Z.D.; Feng, Y.C.; Li, L.; Liao, M.J.; Fu, Y.; Sun, C.X.; Shao, Z.G.; Shen, P.K. Electrochemically synthesized Cu/Pt core-shell catalysts on a porous carbon electrode for polymer electrolyte membrane fuel cells. *J. Power Sources* **2008**, *180*, 84–91. [[CrossRef](#)]
22. Han, L.; Cui, P.; He, H.; Liu, H.; Peng, Z.; Yang, J. A seed-mediated approach to the morphology-controlled synthesis of bimetallic copper–platinum alloy nanoparticles with enhanced electrocatalytic performance for the methanol oxidation reaction. *J. Power Sources* **2015**, *286*, 488–494. [[CrossRef](#)]
23. Xu, D.; Liu, Z.; Yang, H.; Liu, Q.; Zhang, J.; Fang, J.; Zou, S.; Sun, K. Solution-Based Evolution and Enhanced Methanol Oxidation Activity of Monodisperse Platinum–Copper Nanocubes. *Angew. Chem. Int. Ed.* **2009**, *48*, 4217–4221. [[CrossRef](#)] [[PubMed](#)]
24. Hu, C.; Cheng, H.; Zhao, Y.; Hu, Y.; Liu, Y.; Dai, L.; Qu, L. Newly-Designed Complex Ternary Pt/PdCu Nanoboxes Anchored on Three-Dimensional Graphene Framework for Highly Efficient Ethanol Oxidation. *Adv. Mater.* **2012**, *24*, 5493–5498. [[CrossRef](#)] [[PubMed](#)]
25. Gong, M.; Fu, G.; Chen, Y.; Tang, Y.; Lu, T. Autocatalysis and Selective Oxidative Etching Induced Synthesis of Platinum–Copper Bimetallic Alloy Nanodendrites Electrocatalysts. *ACS Appl. Mater. Interfaces* **2014**, *6*, 7301–7308. [[CrossRef](#)] [[PubMed](#)]
26. Fu, G.; Liu, H.; You, N.; Wu, J.; Sun, D.; Xu, L.; Tang, Y.; Chen, Y. Dendritic platinum–copper bimetallic nanoassemblies with tunable composition and structure: Arginine-driven self-assembly and enhanced electrocatalytic activity. *Nano Res.* **2016**, *9*, 755–765. [[CrossRef](#)]
27. Qiu, H.J.; Shen, X.; Wang, J.Q.; Hirata, A.; Fujita, T.; Wang, Y.; Chen, M.W. Aligned Nanoporous Pt–Cu Bimetallic Microwires with High Catalytic Activity toward Methanol Electrooxidation. *ACS Catal.* **2015**, *5*, 3779–3785. [[CrossRef](#)]
28. Zhang, N.; Bu, L.; Guo, S.; Guo, J.; Huang, X. Screw Thread-Like Platinum–Copper Nanowires Bounded with High-Index Facets for Efficient Electrocatalysis. *Nano Lett.* **2016**, *16*, 5037–5043. [[CrossRef](#)]
29. Chen, Z.; Ye, S.; Wilson, A.R.; Ha, Y.-C.; Wiley, B.J. Optically transparent hydrogen evolution catalysts made from networks of copper–platinum core–shell nanowires. *Energy Environ. Sci.* **2014**, *7*, 1461–1467. [[CrossRef](#)]
30. Gong, M.; Yao, Z.; Lai, F.; Chen, Y.; Tang, Y. Platinum–copper alloy nanocrystals supported on reduced graphene oxide: One-pot synthesis and electrocatalytic applications. *Carbon* **2015**, *91*, 338–345. [[CrossRef](#)]
31. Zhang, Z.; Yang, Y.; Nosheen, F.; Wang, P.; Zhang, J.; Zhuang, J.; Wang, X. Fine Tuning of the Structure of Pt–Cu Alloy Nanocrystals by Glycine-Mediated Sequential Reduction Kinetics. *Small* **2013**, *9*, 3063–3069. [[CrossRef](#)] [[PubMed](#)]
32. Luo, S.; Shen, P.K. Concave Platinum–Copper Octopod Nanoframes Bounded with Multiple High-Index Facets for Efficient Electrooxidation Catalysis. *ACS Nano* **2017**, *11*, 11946–11953. [[CrossRef](#)] [[PubMed](#)]
33. Nosheen, F.; Zhang, Z.; Xiang, G.; Xu, B.; Yang, Y.; Saleem, F.; Xu, X.; Zhang, J.; Wang, X. Three-dimensional hierarchical Pt–Cu superstructures. *Nano Res.* **2015**, *8*, 832–838. [[CrossRef](#)]
34. Li, F.; Guo, Y.; Chen, M.; Qiu, H.; Sun, X.; Wang, W.; Liu, Y.; Gao, J. Comparison study of electrocatalytic activity of reduced graphene oxide supported Pt–Cu bimetallic or Pt nanoparticles for the electrooxidation of methanol and ethanol. *Int. J. Hydrogen Energy* **2013**, *38*, 14242–14249. [[CrossRef](#)]
35. Tseng, C.-J.; Lo, S.-T.; Lo, S.-C.; Chu, P.P. Characterization of Pt–Cu binary catalysts for oxygen reduction for fuel cell applications. *Mater. Chem. Phys.* **2006**, *100*, 385–390. [[CrossRef](#)]
36. Eid, K.; Wang, H.; He, P.; Wang, K.; Ahamad, T.; Alshehri, S.M.; Yamauchi, Y.; Wang, L. One-step synthesis of porous bimetallic PtCu nanocrystals with high electrocatalytic activity for methanol oxidation reaction. *Nanoscale* **2015**, *7*, 16860–16866. [[CrossRef](#)] [[PubMed](#)]
37. Cao, X.; Wang, N.; Jia, S.; Shao, Y. Detection of Glucose Based on Bimetallic PtCu Nanochains Modified Electrodes. *Anal. Chem.* **2013**, *85*, 5040–5046. [[CrossRef](#)] [[PubMed](#)]
38. Burpo, F.J.; Nagelli, E.A.; Morris, L.A.; McClure, J.P.; Ryu, M.Y.; Palmer, J.L. Direct solution-based reduction synthesis of Au, Pd, and Pt aerogels. *J. Mater. Res.* **2017**, *32*, 4153–4165. [[CrossRef](#)]
39. Burpo, F.J.; Nagelli, E.A.; Morris, L.A.; McClure, J.P.; Ryu, M.Y.; Palmer, J.L. A Rapid Synthesis Method for Au, Pd, and Pt Aerogels Via Direct Solution-Based Reduction. *JoVE* **2018**, e57875. [[CrossRef](#)]
40. Xiao, X.; Song, H.; Lin, S.; Zhou, Y.; Zhan, X.; Hu, Z.; Zhang, Q.; Sun, J.; Yang, B.; Li, T.; et al. Scalable salt-templated synthesis of two-dimensional transition metal oxides. *Nat. Commun.* **2016**, *7*, 11296. [[CrossRef](#)]
41. Xiao, X.; Yu, H.; Jin, H.; Wu, M.; Fang, Y.; Sun, J.; Hu, Z.; Li, T.; Wu, J.; Huang, L.; et al. Salt-Templated Synthesis of 2D Metallic MoN and Other Nitrides. *ACS Nano* **2017**, *11*, 2180–2186. [[CrossRef](#)] [[PubMed](#)]

42. Burpo, F.J.; Nagelli, E.A.; Winter, S.J.; McClure, J.P.; Bartolucci, S.F.; Burns, A.R.; O'Brien, S.F.; Chu, D.D. Salt-Templated Hierarchically Porous Platinum MacroTube Synthesis. *ChemistrySelect* **2018**, *3*, 4542–4546. [[CrossRef](#)]
43. Burpo, F.J.; Nagelli, E.A.; Mitropoulos, A.N.; Bartolucci, S.F.; McClure, J.P.; Baker, D.R.; Losch, A.R.; Chu, D.D. Salt-templated platinum–palladium porous macrobeam synthesis. *MRS Communications* **2019**, *9*, 280–287. [[CrossRef](#)]
44. Burpo, F.; Nagelli, E.; Morris, L.; Woronowicz, K.; Mitropoulos, A. Salt-Mediated Au-Cu Nanofoam and Au-Cu-Pd Porous Macrobeam Synthesis. *Molecules* **2018**, *23*, 1701. [[CrossRef](#)] [[PubMed](#)]
45. Magnus, G. Ueber einige Verbindungen des Platinchlorürs. *Ann. Phys.* **1828**, *90*, 239–242. [[CrossRef](#)]
46. Vauquelin, N.L. Memoire sur le Palladium et le Rhodium. *Ann. Chim.* **1813**, *88*, 167–198.
47. Wagner, C.D. *NIST X-ray Photoelectron Spectroscopy Database, NIST Standard Reference Database Number 20*; National Institute of Standards and Technology: Gaithersburg, MD, USA, 2000.
48. de Levie, R. On porous electrodes in electrolyte solutions—IV. *Electrochim. Acta* **1964**, *9*, 1231–1245. [[CrossRef](#)]
49. Keiser, H.; Beccu, K.D.; Gutjahr, M.A. Abschätzung der porenstruktur poröser elektroden aus impedanzmessungen. *Electrochim. Acta* **1976**, *21*, 539–543. [[CrossRef](#)]
50. Zhan, D.; Velmurugan, J.; Mirkin, M.V. Adsorption/desorption of hydrogen on Pt nanoelectrodes: evidence of surface diffusion and spillover. *J. Am. Chem. Soc.* **2009**, *131*, 14756–14760. [[CrossRef](#)]
51. Biegler, T.; Rand, D.A.J.; Woods, R. Limiting oxygen coverage on platinized platinum; Relevance to determination of real platinum area by hydrogen adsorption. *J. Electroanal. Chem. Interfacial Electrochem.* **1971**, *29*, 269–277. [[CrossRef](#)]
52. Lai, S.C.S.; Koper, M.T.M. Ethanol electro-oxidation on platinum in alkaline media. *PCCP* **2009**, *11*, 10446–10456. [[CrossRef](#)] [[PubMed](#)]
53. Wang, Y.; Zou, S.; Cai, W.-B. Recent Advances on Electro-Oxidation of Ethanol on Pt- and Pd-Based Catalysts: From Reaction Mechanisms to Catalytic Materials. *Catalysts* **2015**, *5*, 1507–1534. [[CrossRef](#)]
54. Rezaei, M.; Tabaian, S.H.; Haghshenas, D.F. The Role of Electrodeposited Pd Catalyst Loading on the Mechanisms of Formic Acid Electro-Oxidation. *Electrocatalysis* **2014**, *5*, 193–203. [[CrossRef](#)]
55. Schneider, C.A.; Rasband, W.S.; Eliceiri, K.W. NIH Image to ImageJ: 25 years of image analysis. *Nat. Methods* **2012**, *9*, 671–675. [[CrossRef](#)] [[PubMed](#)]



© 2019 by the authors. Licensee MDPI, Basel, Switzerland. This article is an open access article distributed under the terms and conditions of the Creative Commons Attribution (CC BY) license (<http://creativecommons.org/licenses/by/4.0/>).